



Research Article

He-enhanced heterogeneity of radiation-induced segregation in FeNiCoCr high-entropy alloy



W.T. Lin^a, G.M. Yeli^{b,*}, G. Wang^c, J.H. Lin^c, S.J. Zhao^a, D. Chen^{a,d}, S.F. Liu^a, F.L. Meng^e,
Y.R. Li^{a,f}, F. He^a, Y. Lu^{a,g}, J.J. Kai^{a,d,*}

^a Department of Mechanical Engineering, City University of Hong Kong, Hong Kong, China

^b Institute of Nuclear & New Energy Technology, Tsinghua University, Beijing, China

^c Department of Physics, Southern University of Science and Technology, Shenzhen, China

^d Centre for Advanced Nuclear Safety and Sustainable Development, City University of Hong Kong, Hong Kong, China

^e School of Environmental Science and Engineering, Southern University of Science and Technology, Shenzhen, China

^f School of Materials Science and Engineering, Shanghai University, Shanghai, China

^g Nano-Manufacturing Laboratory (NML), City University of Hong Kong Shenzhen Research Institute, Shenzhen, China

ARTICLE INFO

Article history:

Received 18 March 2021

Revised 11 May 2021

Accepted 30 May 2021

Available online 29 July 2021

Keywords:

High-entropy alloy

Radiation-induced segregation

He bubbles

Atom probe tomography

Electron energy-loss spectroscopy

ABSTRACT

Radiation-induced segregation (RIS) is a typical non-equilibrium process that can dramatically alter the behavior of defect sinks and material properties under irradiation. However, RIS mechanisms have been rarely studied around small He bubbles owing to the technical challenges involved in direct measurements of local chemistry. Here, using state-of-the-art atom probe tomography, we report the RIS behavior near He bubbles in the FeNiCoCr high-entropy alloy that indicates Co segregates most strongly, followed by weaker Ni segregation, whereas Fe and Cr are depleted almost to the same degree. Exceptionally, the magnitude of Co segregation around He bubbles is higher than previously measured values at voids and dislocation loops. Electron energy-loss spectroscopy was used to measure the He density and pressure inside individual bubbles. We demonstrate that He bubbles are over-pressurized at the irradiation temperature that could result in the vacancy bias and the subsequent vacancy-dominated RIS mechanism. First-principles calculations further reveal that there are repulsive interactions between He and Co atoms that may reduce the frequency of Co-vacancy exchange. As a result, He atoms likely retard Co diffusion via the vacancy mechanism and enhance the heterogeneity of RIS in Co-containing multicomponent alloys. These insights could provide the basis for understanding He effects in nuclear materials and open an avenue for tailoring the local chemical order of medium-and high-entropy alloys.

© 2022 Published by Elsevier Ltd on behalf of The editorial office of Journal of Materials Science & Technology.

1. Introduction

He accumulation, which can lead to swelling, hardening, and embrittlement of structural materials [1–3], is one of the most daunting challenges for advanced fission and proposed fusion energy systems. One approach for transforming He generation from a liability to an asset is to disperse He atoms and nucleate a high density of He bubbles to serve as sinks [4]. Key benefits of forming abundant He bubbles include: (a) high sink strength promotes vacancy/self-interstitial atom recombination, slowing down vacancy accumulation [5], and (b) intra-crystalline bubbles strongly trap He and prevent it from embrittling grain boundaries. The utilization of He bubbles requires a deep understanding of bubble

formation mechanisms at different levels, including the He diffusion mechanism, kinetics of bubble nucleation and coarsening, and radiation-induced segregation (RIS). However, RIS behavior around small He bubbles is poorly understood, and He effects on RIS mechanisms remain unclear because precise measurements of local chemistry are challenging. Conventional scanning transmission electron microscopy (STEM) spectroscopy, for example, energy-dispersive X-ray spectroscopy and electron energy-loss spectroscopy (EELS), can only provide the average sample composition instead of the accurate composition near He bubbles [6].

Atom probe tomography (APT) is a practical and powerful approach to measure sub-nanometer-scale compositions in three dimensions. The iso-density surfaces have been used to detect He bubbles in APT data [7–9], but producing accurate reconstructions near the bubble structures remains challenging. Recently, based on comprehensive simulations of the field-evaporation process, Wang

* Corresponding authors.

E-mail addresses: ylgm@tsinghua.edu.cn (G.M. Yeli), jijkai@cityu.edu.hk (J.J. Kai).

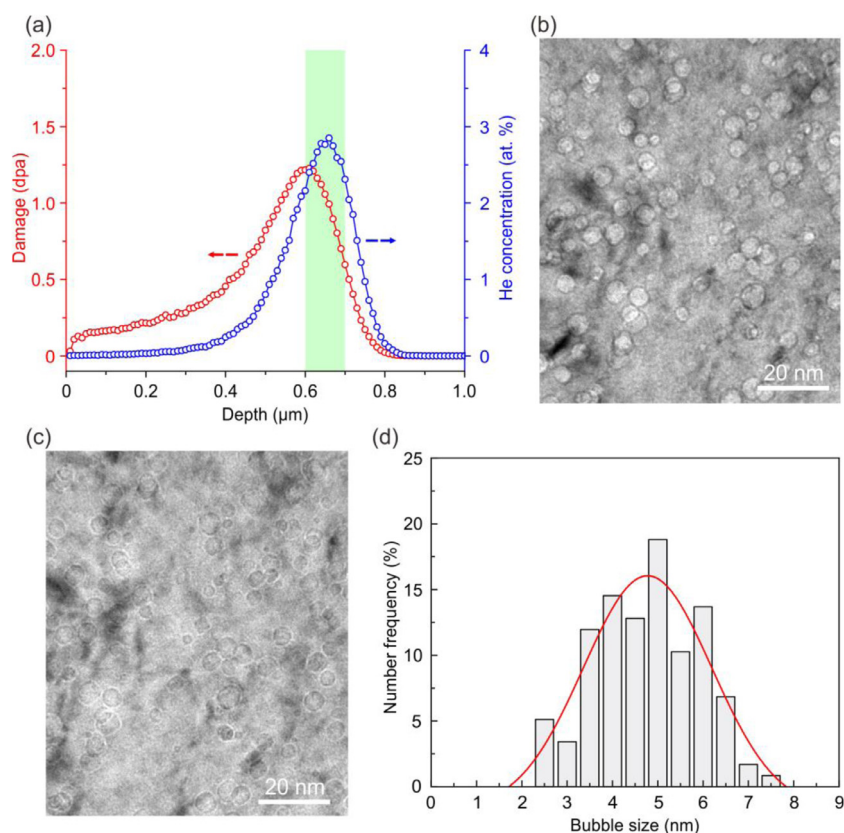


Fig. 1. (a) Predictions of He concentration and damage as a function of depth. The region for further investigation is highlighted. Fresnel-contrast TEM imaging of He bubbles in the FeNiCoCr HEA at (b) under-focus (-300 nm) and (c) over-focus (+300 nm) conditions. (d) Size distribution of He bubbles in the FeNiCoCr HEA irradiated at 873 K.

et al. [10,11] developed a general method for accurately locating the bubble positions within APT data and quantifying the segregation near He bubbles. In this work, we followed the procedure of Wang et al. [11] to perform state-of-the-art APT experiments to study the RIS mechanism near He bubbles in the FeNiCoCr high-entropy alloy (HEA), which is a promising radiation-tolerant structural alloy [12,13] with a sluggish He diffusion nature [14–16]. Compared to RIS at large voids [17] and dislocation loops [18,19], we demonstrate that the enrichment of Co and Ni and the depletion of Fe and Cr are more substantial around He bubbles. Moreover, the magnitude of Co segregation is higher than that of Ni segregation. To determine the dominant mechanism of RIS, STEM-EELS was used to uncover the bubble state at the irradiation temperature (i.e., under-pressurized, at equilibrium pressure, or over-pressurized). Through first-principles calculations, the effects of He atoms on the RIS mechanism around He bubbles are then revealed for the first time.

2. Experimental

2.1. Sample preparation

FeNiCoCr HEA was prepared by arc melting under a high-purity Ar atmosphere. Subsequently, the sample was homogenized at 1373 K for 5 h and water quenched, followed by polishing treatment. The chemical composition of the as-prepared sample measured by APT is listed in Table 1. For simplicity, the low-content impurity elements are ignored in the following. FeNiCoCr HEA was irradiated with 275 keV He⁺ ions at 873 K to a fluence of 5.14×10^{16} ions cm⁻². The beam flux was controlled at 2.8×10^{12} ions cm⁻² s⁻¹. During irradiation, the sample temperature was controlled within an error of ± 5 K, and the chamber vacuum is

Table 1

Measured concentrations of the as-prepared HEA by APT.

Element	Fe	Ni	Co	Cr	C	N
Matrix (at. %)	27.07	22.80	24.27	25.79	0.06	0.01
Error (\pm %)	0.02	0.02	0.02	0.02	0.001	0.001

maintained below 10^{-6} torr. He concentration and displacement damage in the FeNiCoCr HEA were calculated using the Stopping and Range of Ions in Matter (SRIM-2013) code [20] under the quick Kinchin-Pease mode with a displacement threshold energy of 40 eV for all elements [15]. Following He ion irradiation, cross-sectional transmission electron microscopy (TEM) samples were prepared by focused ion beam (FIB) lift-out techniques using an FEI Scios DualBeam SEM/FIB system [21]. Prior to FIB machining, electron beam-induced Pt deposition was performed on the surface of the FeNiCoCr HEA to prevent damage. For the final step, a Ga⁺ ion beam of 2 kV per 8.7 pA was employed to minimize any damaged and amorphous layers generated during high-voltage FIB milling.

2.2. Microstructural characterization

The morphology of He bubbles at the implantation peak region was examined using a JEOL JEM-2100F TEM operated at 200 kV. Fig. 1(a) shows the variations of He concentration and displacements per atom (dpa) with depths ranging from 0 to 1 μ m, where the He peak region for further investigation is highlighted. Fig. 1(b) and (c) displays the Fresnel-contrast TEM images of He bubbles at under-focus and over-focus conditions, and in Fig. 1(d), their size distribution (mean diameter of ~ 4.8 nm) is depicted. The number density of He bubbles (5.7×10^{22} m⁻³) was measured by divid-

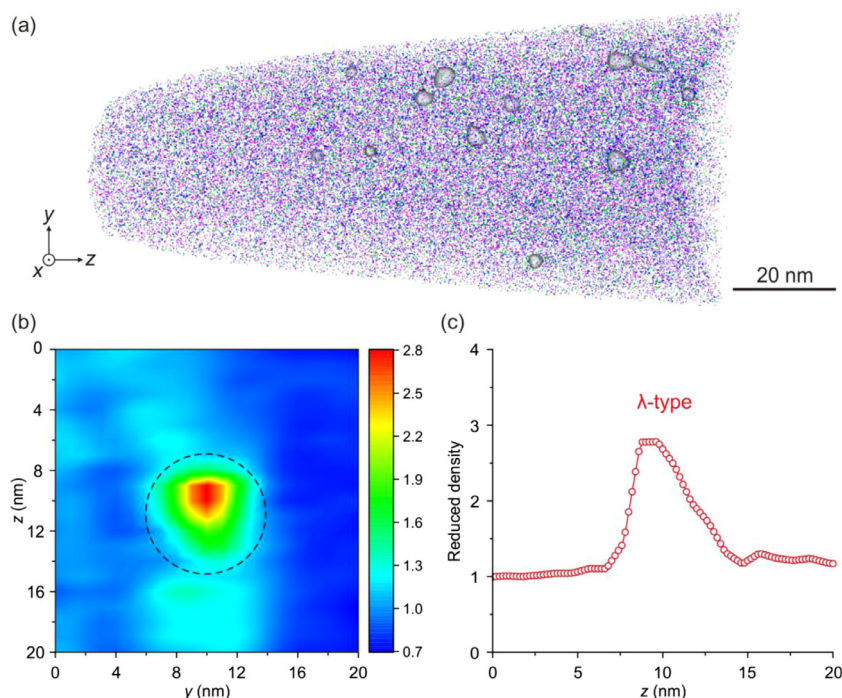


Fig. 2. (a) The variations of atomic density highlighted by 90 atoms nm^{-3} iso-surfaces at the He implantation peak. The λ -type density variation at a bubble location is determined by (b) a two-dimensional density contour plot using a $1 \times 20 \times 20 \text{ nm}^3$ cuboidal region-of-interest and (c) a one-dimensional local density profile using a $1 \times 1 \times 20 \text{ nm}^3$ cuboidal region-of-interest.

ing the total bubble number by the product of the area of TEM observation regions and the TEM sample thickness, which was determined by the EELS log-ratio method [22]. For quantitative composition analysis, the APT needles were prepared by the FEI Scios Dual Beam SEM/FIB system [23] from the He peak region and the un-irradiated region (i.e., $\sim 2 \mu\text{m}$ beneath the surface of the irradiated sample). The APT analysis was conducted using the CAMECA LEAP 5000 XR system with a detection efficiency of 0.52. The specimen was characterized in the laser mode at 60 K with a pulse repetition rate of 200 kHz. A detection rate of 0.005 atoms per pulse and a laser energy of 70 pJ were used. The collected APT data were reconstructed and analyzed using the CAMECA Integrated Visualization and Analysis Software (IVAS) 3.8.2. To investigate the state of He confined in bubbles, spatially resolved EELS was performed using a mono-chromated FEI Titan Cubed Themis G2 300 TEM operated at 60 kV (energy resolution was 0.23 eV) equipped with a Gatan Enfium ERS spectrometer. The spectrum images were acquired with the following conditions: convergence semi-angle of 25 mrad, collection semi-angle of 22.5 mrad, energy dispersion of 0.025 eV per channel, acquisition time of 10 ms per spectrum, and step size of 0.25 nm. The multiple scattering of each spectrum was eliminated by the Fourier-log de-convolution [24], and the contribution of FeNiCoCr HEA was fitted with Gaussian functions by a 10–35 eV window [25]. After subtracting the background signals, the He K-edge can be obtained for calculating the He density and pressure inside bubbles.

3. Results

3.1. RIS around He bubbles

We first determined the positions of He bubbles within the APT reconstruction. Fig. 2(a) shows the atomic map of APT data taken from the He peak region, and iso-density surfaces are utilized to highlight the high-density regions. The two-dimensional density mapping (Fig. 2(b)) and corresponding one-

dimensional density profile (Fig. 2(c)) across a high-density region clearly exhibit the λ -shape variation, i.e., an inverted triangular shape of density variation. According to the criteria given by Wang et al. [11], we then calculate the local charge state ratio $\sigma = \ln[(\text{Ni}^{2+}/\text{Ni}^{1+})_{\text{bubble}}/(\text{Ni}^{2+}/\text{Ni}^{1+})_{\text{matrix}}] = -1.45$, which is consistent with the λ -shape hevariation that originates from a region with a lower evaporation field than the matrix. Thus, the high-density regions indicate the positions of He bubbles in the FeNiCoCr HEA. To validate the accuracy of our measurements, we compared the bubble density obtained by APT ($6.6 \times 10^{22} \text{ m}^{-3}$) with that obtained by TEM imaging ($5.7 \times 10^{22} \text{ m}^{-3}$). The bubble number density measured by APT was estimated using $N = n\eta/N_{\text{tot}}\Omega$ [26], where n is the total number of He bubbles within the APT reconstruction, $\eta = 0.52$ is the detection efficiency of LEAP 5000 XR, N_{tot} is the total number of ranged atoms in the reconstruction, and $\Omega = 1.094 \times 10^{-2} \text{ nm}^3$ is the average atomic volume of FeNiCoCr HEA. We note that APT measurements can only provide a local bubble density due to the small volume of the APT needle. Nevertheless, since two independent approaches yield similar bubble density results, the high-density regions correctly capture He bubbles in the FeNiCoCr HEA.

Fig. 3(a) displays the atomic maps of each element, showing the heterogeneity of elemental compositions at the He peak region. We can clearly identify the segregation of Co and Ni with the depletion of Fe and Cr near He bubbles. To exclude the possibility that the observed segregations were introduced by incipient concentration waves [27], we also performed APT measurements of the un-irradiated region (Fig. 3(b)), i.e., $\sim 2 \mu\text{m}$ beneath the surface of the irradiated sample, where no chemical segregations were observed. Fig. 3(c) shows the one-dimensional concentration profile across the He bubble determined in Fig. 2(b) and (c). More concentration profiles across other He bubbles are shown in Supplementary Fig. S1, exhibiting similar segregation phenomena. Our statistical results demonstrate that Co segregates most strongly (increasing from 24.3 at.% to 37.7 ± 2.3 at.%), followed by weaker Ni segregation (increasing from 22.8 at.% to 31.8 ± 2.1 at.%), while Fe (de-

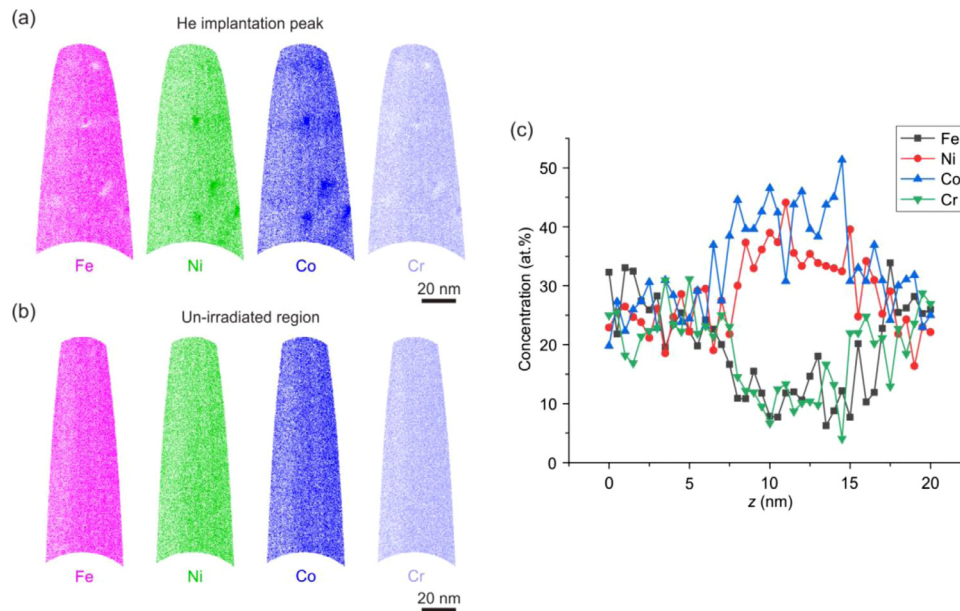


Fig. 3. Atom maps of Fe, Ni, Co, and Cr in the samples from (a) the He implantation peak and (b) the un-irradiated region, i.e., $\sim 2 \mu\text{m}$ beneath the surface of the irradiated sample. The thickness of the slices is 2 nm. (c) One-dimensional concentration profiles across the He bubble determined in Fig. 2(b) and (c), obtained by calculating element concentrations in 0.5 nm-wide bins from a cylindrical region-of-interest.

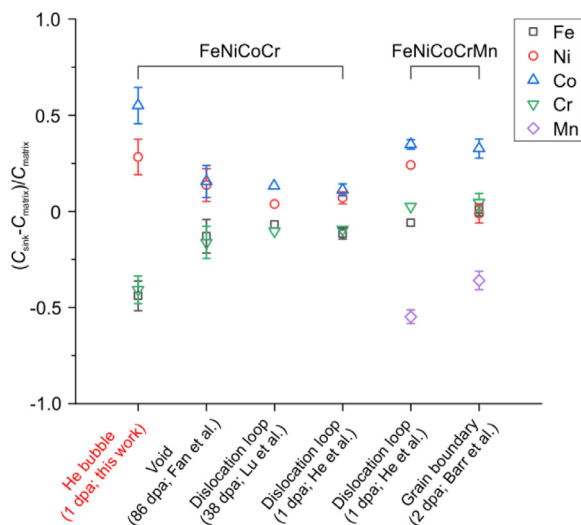


Fig. 4. Comparison in the magnitude of RIS, i.e., change in composition relative to that in the un-irradiated matrix, at He bubbles (this work), voids [17], and dislocation loops [18,19] in FeNiCoCr HEAs. The data of RIS at dislocation loops [18] and grain boundaries [28] in FeNiCoCrMn HEAs are also included.

creasing from 27.1 at.% to 15.2 ± 2.1 at.%) and Cr (decreasing from 25.8 at.% to 15.3 ± 1.8 at.%) deplete almost to the same degree. Compared to the magnitude of RIS measured at voids [17] and dislocation loops [18,19] in the FeNiCoCr HEA, Co enrichment around He bubbles is significantly stronger, as demonstrated in Fig. 4. The magnitude of Co segregation around He bubbles is even higher than those measured at dislocation loops [18] and grain boundaries [28] in the FeNiCoCrMn HEA, in which fast Mn diffusion enhances the enrichment of Co [29].

3.2. He density and pressure inside bubbles

To explore the RIS mechanism around He bubbles, we then investigated the state of bubbles of different diameters by STEM-EELS. Fig. 5(a) shows the high-angle annular dark-field (HAADF)

STEM image of He bubbles in the FeNiCoCr HEA. Owing to the weak scattering power of He atoms [30], He bubbles can be considered as spherical voids in HAADF imaging, and thus the darker regions indicate the positions of He bubbles. The He chemical map is displayed as an inset in Fig. 5(a), which is obtained by integrating the intensity of He K edge at each probe position. It shows excellent agreement with the positions of He bubbles in the HAADF image. Fig. 5(b) compares the EELS spectra acquired from the center of a He bubble and from the adjacent matrix, where a clear He K edge can be observed. The density of He atoms n_{He} inside bubbles was calculated by the relation [31]: $n_{\text{He}} = I_p / \sigma_p I_z d$, where I_p is the integrated intensity of He K edge, $\sigma_p = 1.286 \times 10^{-23} \text{ m}^2$ is the cross-section for the He $1s \rightarrow 2p$ transition under our experimental conditions calculated by the equations of Walsh et al. [31], I_z is the integrated intensity of the zero-loss peak, and d is the bubble diameter. The estimated He densities in bubbles of ~ 3.9 – 6.2 nm diameters are in the range of ~ 56 – 79 nm^{-3} , as shown in Fig. 6(a). The data obtained from Ni after He ion irradiation at 773 K [32] and PE16 alloy (a Ni-Fe-Cr base alloy) after neutron irradiation at 823 K [31,33] are also displayed. He bubbles in the FeNiCoCr HEA are smaller than those in Ni and PE16 alloys and thus have higher He densities.

At high He densities, it is not possible to calculate the pressure inside He bubbles using neither the ideal gas nor the van der Waals gas law. For describing the thermodynamic behavior at high atomic densities, the equation of state of He given by Korbeek and Schouten [34] was utilized to estimate the He pressure. Fig. 6(b) shows the pressure inside bubbles in the FeNiCoCr HEA at the implantation temperature. At thermodynamic equilibrium, the pressure inside a bubble is expected to be $P = 2\gamma/r$, where γ is the surface free energy and r is the bubble radius. The surface energy γ for the FeNiCoCr HEA is estimated to be about 2.3 J m^{-2} , which was calculated by averaging the surface energy of each element ($\gamma = \sim 2.34 \text{ J m}^{-2}$ for Fe, $\sim 2.30 \text{ J m}^{-2}$ for Ni, $\sim 2.44 \text{ J m}^{-2}$ for Co and $\sim 2.26 \text{ J m}^{-2}$ for Cr [35]). We show that He pressures inside the bubbles of ~ 3.9 – 6.2 nm diameters are higher than the equilibrium pressure, and thus He bubbles are over-pressurized at the implantation temperature. Owing to the surrounding compressive stress fields, the over-pressurized He bubbles are biased sinks for

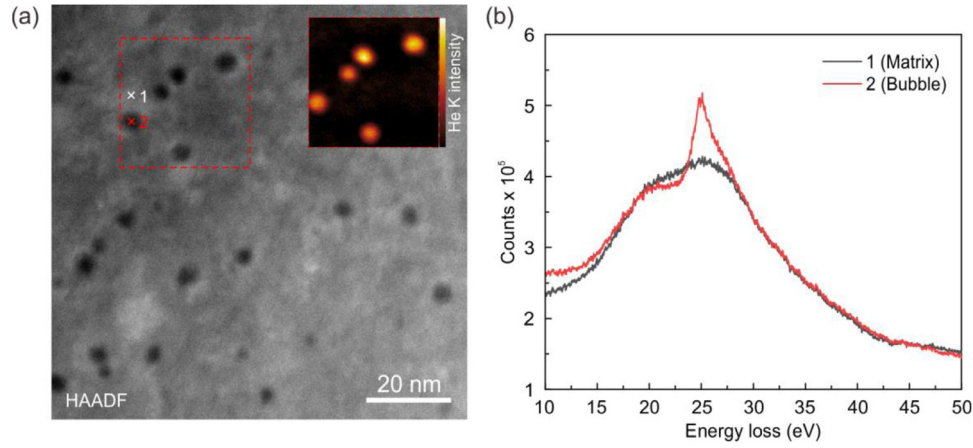


Fig. 5. (a) HAADF STEM image of He bubbles in the FeNiCoCr HEA. The inset is the corresponding He chemical map of the red rectangular area. (b) EELS spectra collected from the matrix (position 1) and the He bubble (position 2) marked in (a).

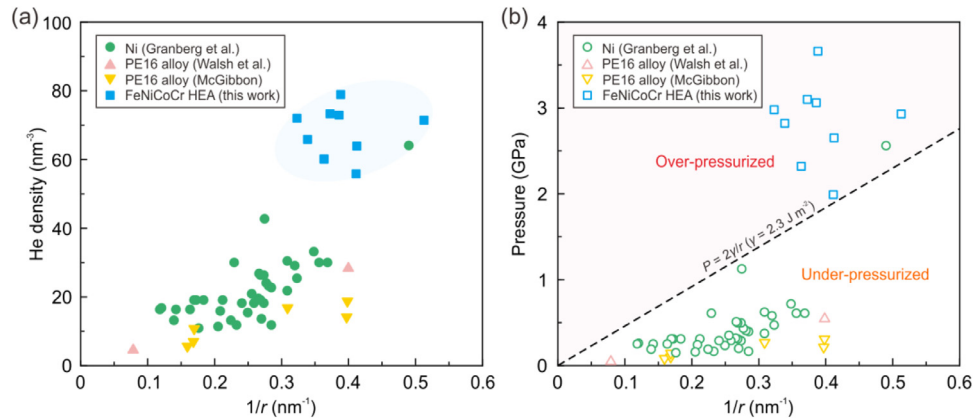


Fig. 6. (a) The estimated He density as a function of the inverse radii. (b) The pressure inside He bubbles in the FeNiCoCr HEA at 873 K as a function of the inverse radii. Also shown is the line $P = 2\gamma/r$ with the γ of 2.3 J m^{-2} for the FeNiCoCr HEA. Data of He density and pressure obtained from Ni by Granberg et al. [32] and PE16 alloys by Walsh et al. [31] and McGibbon [33] are also displayed.

vacancies [36–38], and the vacancy mechanism could play a dominant role in RIS.

4. Discussion

4.1. Modeling RIS near He bubbles

For explaining the unusual RIS behavior around He bubbles, we first compared model predictions to the present experimental segregation data. Two mechanisms have been proposed to explain the RIS behavior in binary and ternary alloys, i.e., the inverse Kirkendall effect [39,40] and interstitial binding [41]. Recently, these mechanisms were also used to explain the RIS behavior in HEAs [18,19,28,42]. To model the direction and amount of segregation based on the vacancy-dominated inverse Kirkendall effect, we calculated the discriminant (M_j) of RIS [43] for an element j ($= \text{Fe, Ni, Co, Cr}$):

$$M_j = \frac{\nabla C_j}{\nabla C_v} = \frac{\frac{d_{jv}C_j}{D_j} \sum_{k \neq j} \frac{d_{ki}C_k}{D_k} - \frac{d_{ji}C_j}{D_j} \sum_{k \neq j} \frac{d_{kv}C_k}{D_k}}{\alpha \sum_k \frac{d_{ki}C_k}{D_k}} \quad (1)$$

where C_j is the concentration of element j , D_j ($= d_{jv}C_v + d_{ji}C_i$) is the total diffusivity of the element j , C_v and C_i are the concentrations of vacancies and interstitials, respectively, d_{jv} and d_{ji} are the partial diffusion coefficients of the element j via vacancies and interstitials, respectively, and α is the thermodynamic factor [44]. Here, the vacancy concentration C_v around a perfect sink at

Table 2

Parameters for RIS discriminant (M_j) calculations.

	$j = \text{Fe}$	$j = \text{Ni}$	$j = \text{Co}$	$j = \text{Cr}$
C_j	0.271	0.228	0.243	0.258
k (eV/K)	$8.617333262145 \times 10^{-5}$			
T (K)	873			
E_v^f (eV) [46]	1.831			
E_{jv} (eV) [47]	0.799	1.021	0.982	0.587
α [44]	1			

equilibrium [45] is estimated as $3\exp(-E_v^f/kT)$, where E_v^f is the vacancy formation energy obtained by first-principle calculations [46], k is the Boltzmann constant, and T is the irradiation temperature. The partial diffusion coefficient d_{jv} of the element j via vacancies is estimated as $\exp(-E_{jv}/kT)$, where E_{jv} is the vacancy migration energy obtained by first-principles calculations [47]. For solely modeling the inverse Kirkendall effect, the interstitial concentration C_i is taken as 0 [43], and the partial diffusion coefficient via interstitials d_{ji} was set to be equal for every element. The detailed parameters used for the calculations are listed in Table 2, and then, $M_{\text{Fe}} = 2.83 \times 10^9$, $M_{\text{Ni}} = -5.51 \times 10^9$, $M_{\text{Co}} = -3.99 \times 10^8$, and $M_{\text{Cr}} = 2.83 \times 10^9$ are obtained. Since the vacancy concentration decreases toward a sink [48], i.e., $\nabla C_v > 0$, a positive M value indicates the depletion of an element, while a negative M value indicates the enrichment of an element. The discriminant reveals that Ni and Co enrich, whereas Fe and Cr deplete near He bubbles,

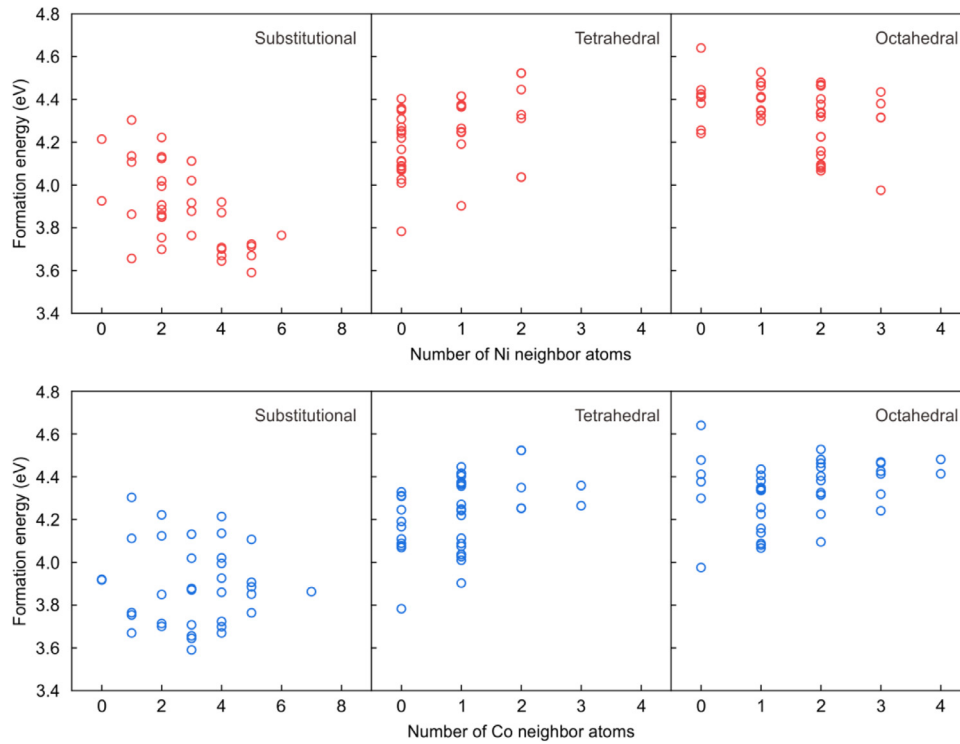


Fig. 7. Relationships between formation energies of a single He atom in the FeNiCoCr HEA at substitutional, octahedral, and tetrahedral positions and the number of Ni/Co neighboring atoms surrounding the He atom. The data are plotted according to the re-analysis of our previous first-principles results [14].

Table 3
Atomic radius (R) of all elements [49].

	Fe	Ni	Co	Cr
R (Å)	1.274	1.246	1.252	1.282

agreeing with our experimental data. Moreover, $|M_{\text{Fe}}/M_{\text{Cr}}| = 1$ and $|M_{\text{Ni}}/M_{\text{Co}}| > 1$, suggesting that Fe depletion is similar to Cr depletion, and Ni enrichment is stronger than Co enrichment. The theoretical predictions of the amount of Fe/Cr depletion are consistent, but the predictions of the amount of Ni/Co segregation are contradictory to our APT results. We then predict the RIS behavior according to the interstitial binding mechanism, which is governed by the difference of atomic size (R). Since $R_{\text{Cr}} > R_{\text{Fe}} > R_{\text{Co}} > R_{\text{Ni}}$ [49] (see Table 3), the larger Cr and Fe atoms are not favored, while the smaller Co and Ni atoms are favored around He bubbles, in agreement with our observations. However, Ni should be more enriched since the interstitial diffusion is dominated by the undersized Ni atoms [18,19]. It appears that both two mechanisms cannot predict abnormal Co segregation without considering He effects. In other words, these analyses indicate that the strong Co segregation may be related to He atoms, which could influence the elemental diffusion behavior around He bubbles.

4.2. An atomistic mechanism of He-enhanced heterogeneity of RIS

We now reveal the atomic-scale mechanism associated with He that results in the difference in the diffusivities of elements and the unusual RIS behavior around He bubbles. In light of the vacancy-dominated RIS mechanism demonstrated above, we carefully re-analyzed our previous first-principles results of He (can be regarded as the He-vacancy complex) behavior in the FeNiCoCr HEA [14]. Interestingly, the results show that He atoms usually possess higher formation energies when their surroundings contain more Co atoms in substitutional and interstitial (tetrahedral

and octahedral) positions (Fig. 7). In contrast, the formation energies of He atoms are lower when their local environment contains more Ni atoms at substitutional and octahedral positions. Therefore, there are repulsive interactions between the He and Co atoms and attractive interactions between the He and Ni atoms. The repulsive forces may reduce the probability of formation of He-Co complexes and the frequency of Co-vacancy exchange. Therefore, the He-induced slowing of Co diffusion via the vacancy mechanism results in strong Co segregation near He bubbles. An understanding of the He-enhanced heterogeneity of RIS around He bubbles provides essential information for predicting the kinetics of He bubble growth in Co-containing multicomponent alloys and for designing alloys with superior resistance to He-induced hardening and embrittlement. Future studies will be needed to quantify the extent of Co diffusion retardation induced by He atoms and to explore the effects of He on the possible RIS behavior around special bubble structures, for example, He platelets [50] and He bubble superlattices [51].

4.3. Implications for stacking fault energy fluctuations

We finally discuss the implications for stacking fault energy (SFE) fluctuations in medium- and high-entropy alloys. It is known that the variations of local chemical order can directly tune the SFE [52,53], which further influences the irradiation performance and mechanical properties of alloys. Based on the model proposed by Olson and Cohen [54], the ideal SFE at the matrix and near He bubbles (Fig. 8) can be calculated as [55]: $\gamma_{\text{SFE}} = 2\rho\Delta G^{\gamma \rightarrow \epsilon} + 2\sigma$, where $\rho = \frac{4}{\sqrt{3}} \frac{1}{a^2 N} = 2.95 \times 10^{-5} \text{ mol m}^{-2}$ is the molar surface density along {111} planes ($a = 0.3604 \text{ nm}$ [56] is the lattice constant and $N = 6.022 \times 10^{23} \text{ mol}^{-1}$ is the Avogadro number), $\Delta G^{\gamma \rightarrow \epsilon}$ is the difference in molar Gibbs energy of the hexagonal close-packed (HCP) and face-centered cubic (FCC) phases, and $\sigma = 10 \text{ mJ m}^{-2}$ [57] is the interfacial energy between FCC and HCP phases. The term $\Delta G^{\gamma \rightarrow \epsilon}$ was calculated by the CALPHAD (Calcu-

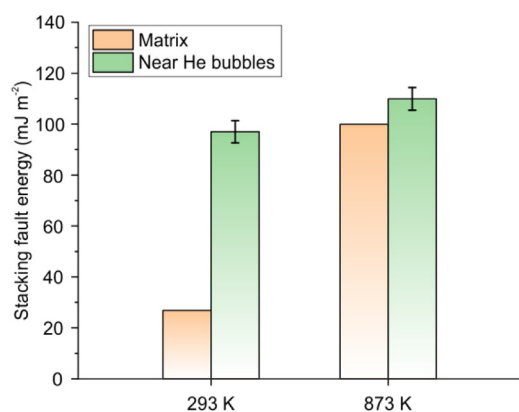


Fig. 8. Stacking fault energy of the matrix and near He bubbles at room temperature and irradiation temperature. The error bars indicate the standard deviation of the calculated SFE near 10 different He bubbles.

lation of Phase Diagrams) software Thermo-Calc (database: TTN18) according to the experimentally measured compositions (Fig. 3 and Supplementary Fig. S1). At the irradiation temperature, the SFE near He bubbles ($109.9 \pm 4.4 \text{ mJ m}^{-2}$) is a little higher than that of the matrix (99.9 mJ m^{-2}). Whereas, at room temperature, the SFE near He bubbles ($97.0 \pm 4.4 \text{ mJ m}^{-2}$) is more than triple the value of the matrix (26.9 mJ m^{-2}), which is in agreement with the experimental range of $27\text{--}32.5 \text{ mJ m}^{-2}$ [56,58]. Our calculations indicate that the RIS-induced local chemical order gives rise to the higher SFE near He bubbles in the FeNiCoCr HEA. Such SFE fluctuations could improve the irradiation tolerance of multicomponent alloys [59,60] and enhance the cross-slip around He bubbles for strain hardening of alloys [61,62]. This finding also supports the critical role of high He pressures in triggering the partial dislocation emission from pressurized He bubbles in the FeNiCoCr HEA [63].

5. Conclusions

To conclude, using state-of-the-art APT analysis, we quantified the radiation-induced variation of local chemistry around He bubbles in the FeNiCoCr HEA. Co segregates most strongly (increasing by $13.4 \pm 2.3 \text{ at.}\%$), followed by weaker Ni segregation (increasing by $9.0 \pm 2.1 \text{ at.}\%$), while Fe (decreasing by $11.9 \pm 2.1 \text{ at.}\%$) and Cr (decreasing by $10.5 \pm 1.8 \text{ at.}\%$) are depleted almost to the same degree. By combining STEM-EELS analysis and first-principles calculations, we demonstrate for the first time that He atoms can decrease Co diffusion via the vacancy mechanism and promote Co segregation around He bubbles. Our results indicate that He atoms can enhance the heterogeneity of diffusivities in Co-containing multicomponent alloys and that the effects of He on RIS mechanisms should be considered in the future. More importantly, such a mechanism provides another route for tuning the local chemical order and stacking fault energy of medium- and high-entropy alloys.

Declaration of Competing Interests

The authors declare that they have no known competing financial interests or personal relationships that could have appeared to influence the work reported in this paper.

Acknowledgments

The authors would like to thank Dr. H. Niu and Mr. H.K. You at NTHU for their assistance in He⁺ ion irradiation. J.J.K. acknowledges the funding support from the Hong Kong Research Grant

Council (Grant Nos. CityU11214820 and CityU11205018). Y.L. acknowledges the funding support from the National Natural Science Foundation of China (NSFC) under project 11922215. F.L.M. acknowledges the funding support from the Natural Science Foundation of Guangdong Province in China (Grant No. 2019A1515011836). G.W. and J.H.L. would like to acknowledge the support from National Natural Science Foundation of China (Grant No. 11974156), Guangdong International Science Collaboration Project (Grant No. 2019A050510001), and the assistance of SUSTech Core Research Facilities, especially technical support from Pico-Centre.

Supplementary materials

Supplementary material associated with this article can be found, in the online version, at doi:10.1016/j.jmst.2021.05.053.

References

- [1] S.J. Zinkle, J.T. Busby, *Mater. Today* 12 (2009) 12–19.
- [2] S.J. Zinkle, G.S. Was, *Acta Mater.* 61 (2013) 735–758.
- [3] Y. Lu, H. Huang, X. Gao, C. Ren, J. Gao, H. Zhang, S. Zheng, Q. Jin, Y. Zhao, C. Lu, T. Wang, T. Li, *J. Mater. Sci. Technol.* 35 (2019) 369–373.
- [4] S.J. Zinkle, L.L. Snead, *Annu. Rev. Mater. Res.* 44 (2014) 241–267.
- [5] G.R. Odette, P. Miao, D.J. Edwards, T. Yamamoto, R.J. Kurtz, H. Tanigawa, *J. Nucl. Mater.* 417 (2011) 1001–1004.
- [6] C.B. Carter, D.B. Williams, *Transmission Electron Microscopy: Diffraction, Imaging, and Spectrometry*, Springer, 2016.
- [7] M.K. Miller, L. Longstreth-Spoor, K.F. Kelton, *Ultramicroscopy* 111 (2011) 469–472.
- [8] P.D. Edmondson, C.M. Parish, Y. Zhang, A. Hallén, M.K. Miller, *J. Nucl. Mater.* 434 (2013) 210–216.
- [9] M.J. Lloyd, R.G. Abernethy, M.R. Gilbert, I. Griffiths, P.A.J. Bagot, D. Nguyen-Manh, M.P. Moody, D.E.J. Armstrong, *Scr. Mater.* 173 (2019) 96–100.
- [10] X. Wang, K. Jin, D. Chen, H. Bei, Y. Wang, W.J. Weber, Y. Zhang, J. Poplawsky, K.L. More, *Microsc. Microanal.* 25 (2019) 1558–1559.
- [11] X. Wang, C. Hatzoglou, B. Sneed, Z. Fan, W. Guo, K. Jin, D. Chen, H. Bei, Y. Wang, W.J. Weber, Y. Zhang, B. Gault, K.L. More, F. Vurpillot, J.D. Poplawsky, *Nat. Commun.* 11 (2020) 1–11.
- [12] C. Lu, L. Niu, N. Chen, K. Jin, T. Yang, P. Xiu, Y. Zhang, F. Gao, H. Bei, S. Shi, M.-R. He, I.M. Robertson, W.J. Weber, L. Wang, *Nat. Commun.* 7 (2016) 13564.
- [13] Y. Lin, T. Yang, L. Lang, C. Shan, H. Deng, W. Hu, F. Gao, *Acta Mater.* 196 (2020) 133–143.
- [14] S. Zhao, D. Chen, J.J. Kai, *Mater. Res. Lett.* 7 (2019) 188–193.
- [15] D. Chen, S. Zhao, J. Sun, P. Tai, Y. Sheng, Y. Zhao, G. Yeli, W. Lin, S. Liu, W. Kai, J. Kai, *J. Nucl. Mater.* 526 (2019) 151747.
- [16] D. Chen, S. Zhao, J. Sun, P. Tai, Y. Sheng, G. Yeli, Y. Zhao, S. Liu, W. Lin, W. Kai, J. Kai, *J. Nucl. Mater.* 542 (2020) 152458.
- [17] Z. Fan, T. Yang, B. Kombaiah, X. Wang, P.D. Edmondson, Y.N. Osetsky, K. Jin, C. Lu, H. Bei, L. Wang, K.L. More, W.J. Weber, Y. Zhang, *Materialia* 9 (2020) 100603.
- [18] M.-R. He, S. Wang, S. Shi, K. Jin, H. Bei, K. Yasuda, S. Matsumura, K. Higashida, I.M. Robertson, *Acta Mater.* 126 (2017) 182–193.
- [19] C. Lu, T. Yang, K. Jin, N. Gao, P. Xiu, Y. Zhang, F. Gao, H. Bei, W.J. Weber, K. Sun, Y. Dong, L. Wang, *Acta Mater.* 127 (2017) 98–107.
- [20] J.F. Ziegler, M.D. Ziegler, J.P. Biersack, *Nucl. Instruments Methods Phys. Res. Sect. B Beam Interact. with Mater. Atoms* 268 (2010) 1818–1823.
- [21] W. Lin, S. Liu, D. Chen, C. Dang, H. Niu, Y. Zhao, B. Han, Y. Lu, J.-J. Kai, *Mater. Lett.* 250 (2019) 68–71.
- [22] T. Malis, S.C. Cheng, R.F. Egerton, *J. Electron Microscop.* 8 (1988) 193–200.
- [23] G. Yeli, D. Chen, K. Yabuuchi, A. Kimura, S. Liu, W. Lin, Y. Zhao, S. Zhao, J.J. Kai, *J. Nucl. Mater.* 540 (2020) 152364.
- [24] R.F. Egerton, *Electron Energy-Loss Spectroscopy in the Electron Microscope*, Springer Science & Business Media, 2011.
- [25] S. Fréchet, M. Walls, M. Kociak, J.P. Chevalier, J. Henry, D. Gorse, *J. Nucl. Mater.* 393 (2009) 102–107.
- [26] G. Yeli, M.A. Auger, K. Wilford, G.D.W. Smith, P.A.J. Bagot, M.P. Moody, *Acta Mater.* 125 (2017) 38–49.
- [27] Q. Ding, Y. Zhang, X. Chen, X. Fu, D. Chen, S. Chen, L. Gu, F. Wei, H. Bei, Y. Gao, M. Wen, J. Li, Z. Zhang, T. Zhu, R.O. Ritchie, Q. Yu, *Nature* 574 (2019) 223–227.
- [28] C.M. Barr, J.E. Nathaniel II, K.A. Unocic, J. Liu, Y. Zhang, Y. Wang, M.L. Taheri, *Scr. Mater.* 156 (2018) 80–84.
- [29] M. Vaidya, K.G. Pradeep, B.S. Murty, G. Wilde, S.V. Divinski, *Acta Mater.* 146 (2018) 211–224.
- [30] N. Tanaka, *Scanning Transmission Electron Microscopy of Nanomaterials*, World Scientific, 2015.
- [31] C.A. Walsh, J. Yuan, L.M. Brown, *Philos. Mag. A* 80 (2000) 1507–1543.
- [32] F. Granberg, X. Wang, D. Chen, K. Jin, Y. Wang, H. Bei, W.J. Weber, Y. Zhang, K.L. More, K. Nordlund, F. Djurabekova, *Scr. Mater.* 191 (2021) 1–6.
- [33] A.J. McGibbon, *Inst. Phys. Conf. Ser.* (1991) 109–112.
- [34] P.J. Kortbeek, J.A. Schouten, *J. Chem. Phys.* 95 (1991) 4519–4524.
- [35] W.R. Tyson, W.A. Miller, *Surf. Sci.* 62 (1977) 267–276.

- [36] R.D.S. Yadava, J. Nucl. Mater. 98 (1981) 47–62.
- [37] V.A. Borodin, A.I. Ryazanov, C. Abromeit, J. Nucl. Mater. 207 (1993) 242–254.
- [38] F. Wu, Y. Zhu, Q. Wu, X. Li, P. Wang, H. Wu, J. Nucl. Mater. 496 (2017) 265–273.
- [39] P.R. Okamoto, L.E. Rehn, J. Nucl. Mater. 83 (1979) 2–23.
- [40] T.R. Allen, J.T. Busby, G.S. Was, E.A. Kenik, J. Nucl. Mater. 255 (1998) 44–58.
- [41] H. Wiedersich, P.R. Okamoto, N.Q. Lam, J. Nucl. Mater. 83 (1979) 98–108.
- [42] Z. Fan, W. Zhong, K. Jin, H. Bei, Y.N. Osetsky, Y. Zhang, J. Mater. Res. (2021) 1–13.
- [43] S. Watanabe, H. Takahashi, J. Nucl. Mater. 208 (1994) 191–194.
- [44] B. Kombaiiah, P.D. Edmondson, Y. Wang, L.A. Boatner, Y. Zhang, J. Nucl. Mater. 514 (2019) 139–147.
- [45] A.D. Marwick, J. Nucl. Mater. 135 (1985) 68–76.
- [46] S. Zhao, T. Egami, G.M. Stocks, Y. Zhang, Phys. Rev. Mater. 2 (2018) 013602.
- [47] G. Veliša, E. Wendler, S. Zhao, K. Jin, H. Bei, W.J. Weber, Y. Zhang, Mater. Res. Lett. 6 (2018) 136–141.
- [48] A.J. Ardell, P. Bellon, Curr. Opin. Solid State Mater. Sci. 20 (2016) 115–139.
- [49] C.H. Suresh, N. Koga, J. Phys. Chem. A 105 (2001) 5940–5944.
- [50] J. Chen, P. Jung, H. Trinkaus, Phys. Rev. Lett. 82 (1999) 2709.
- [51] R.W. Harrison, G. Greaves, H. Le, H. Bei, Y. Zhang, S.E. Donnelly, Curr. Opin. Solid State Mater. Sci. 23 (2019) 100762.
- [52] J. Ding, Q. Yu, M. Asta, R.O. Ritchie, Proc. Natl. Acad. Sci. U. S. A. 115 (2018) 8919–8924.
- [53] R. Zhang, S. Zhao, J. Ding, Y. Chong, T. Jia, C. Ophus, M. Asta, R.O. Ritchie, A.M. Minor, Nature 581 (2020) 283–287.
- [54] G.B. Olson, M. Cohen, Metall. Trans. A 7 (1976) 1897–1904.
- [55] S. Curtze, V.-T. Kuokkala, A. Oikari, J. Talonen, H. Hänninen, Acta Mater. 59 (2011) 1068–1076.
- [56] Y. Wang, B. Liu, K. Yan, M. Wang, S. Kabra, Y.-L. Chiu, D. Dye, P.D. Lee, Y. Liu, B. Cai, Acta Mater. 154 (2018) 79–89.
- [57] Z. Li, D. Raabe, JOM 69 (2017) 2099–2106.
- [58] S.F. Liu, Y. Wu, H.T. Wang, J.Y. He, J.B. Liu, C.X. Chen, X.J. Liu, H. Wang, Z.P. Lu, Intermetallics 93 (2018) 269–273.
- [59] S. Zhao, J. Nucl. Mater. 530 (2020) 151886.
- [60] N. Hashimoto, T. Fukushi, E. Wada, W.Y. Chen, J. Nucl. Mater. 545 (2021) 152642.
- [61] M.A. Meyers, K.K. Chawla, Mechanical Behavior of Materials, Cambridge University Press, 2008.
- [62] T. Hatano, T. Kaneko, Y. Abe, H. Matsui, Phys. Rev. B 77 (2008) 64108.
- [63] W.T. Lin, D. Chen, C.Q. Dang, P.J. Yu, G. Wang, J.H. Lin, F.L. Meng, T. Yang, Y.L. Zhao, S.F. Liu, J.P. Du, G.M. Yeli, C.T. Liu, Y. Lu, S. Ogata, J.J. Kai, Acta Mater. 210 (2021) 116843.